Reciprocity Theory of Apertureless Scanning Near-Field Optical Microscopy with Point-Dipole Probes

Moritz Esslinger* **and Ralf Vogelgesang**

Max Planck Institute for Solid State Research, Stuttgart, Germany

ABSTRACT Near-field microscopy offers the opportunity to reveal optical contrast at deep subwavelength scales. In scanning near-field optical microscopy (SNOM), the diffraction limit is overcome by a nanoscopic probe in close proximity to the sample. The interaction of the probe with the sample fields necessarily perturbs the bare sample response, and a critical issue is the interpretation of recorded signals. For a few specific SNOM configurations, individual descriptions have been modeled, but a general and intuitive framework is still lacking. Here, we give an exact formulation of the measurable signals in SNOM which is easily applicable to experimental configurations. Our results are in close analogy with the description Tersoff and Hamann have derived for the tunneling currents in scanning tunneling microscopy. For point-like scattering probe tips, such as used in apertureless SNOM, the theory simplifies dramatically to a single scalar relation. We find that the measured signal is directly proportional to the field of the coupled tip—sample system at the position of the tip. For weakly interacting probes, the model thus verifies the empirical findings that the recorded signal is proportional to the unperturbed field of the bare sample. In the more general case, it provides guidance to an intuitive and faithful interpretation of recorded images, facilitating the characterization of tip-related distortions and the evaluation of novel SNOM configurations, both for aperture-based and apertureless SNOM.

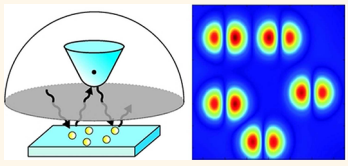

KEYWORDS: imaging theory · reciprocity theorem · Born series interaction · apertureless near-field microscopy · SNOM

Since the advent of nanotechnology, the exploration of nanoscopic structures continues to spur new developments in all areas of the natural sciences, ranging from research on their fundamental properties to ultrasensitive detectors, subwavelength light management, biomedical diagnostics and therapeutics, *etc.*[1−10] Especially, where this concerns optical phenomena, a key role is played by microscopy techniques capable of spatial resolution at the nanometer scale. This appears to be an unreachable goal with conventional diffraction-limited imaging techniques, which offer hardly better than half a wavelength resolution. However, a variety of significant technological advances in both electronic and optical near-field microscopies now offer routine discrimination of optical features smaller than 10 nm.[11]

Unfortunately, this high-resolution contrast does not necessarily come with easy, faithful interpretation of recorded images. To beat the diffraction limit, the evanescent near-fields must be accessed by some kind of (scanning) probe.[12] The intricate interaction between an unknown sample under study and the probe is all but fully understood. A detailed model for recorded signals would also be very beneficial in inverse scattering problems.[13,14] Here we concentrate on scanning near-field optical microscopy. For a handful of special cases, successful models are available, which represent the signal measured in terms of easily understood quantities.[15−17] A general theory for SNOM, based on the Maxwell equations, is also available.[18] In this framework, the measured signal can be calculated by integrating over an infinite plane, separating tip and sample.

The current situation in SNOM is somewhat reminiscent of scanning tunneling microscopy (STM) in the early 1980s. *Ab initio* theories were available but cumbersome to use, and simplified models based on *ad hoc* assumptions often led to paradoxical interpretations. This changed when Tersoff and Hamann provided their celebrated interpretation framework,[19,20] which allowed scanning tunneling microscopy images to be easily interpreted with certainty and largely without *a priori* knowledge or further simulations.

In STM, the interpretation of recorded signals is based on Bardeen's formula for the current across a tunneling barrier.[21] It presumes weak coupling between the two electrodes referred to as "sample" and "tip". Weak coupling is appropriate for electronic states that decay evanescently into the gap between the electrodes. Tersoff and Hamann proceeded by introducing the simplest conceivable model for a tip, namely, a point-like s-wave emitter. Their elegant

* Address correspondence to m.esslinger@fkf.mpg.de.

Received for review June 27, 2012 and accepted August 16, 2012.

Published online August 17, 2012
10.1021/nn302864d

analytical expression for the tunneling current showed it is simply proportional to the wave function of the bare sample at the location of the point-like tip.

Some of the earliest results in SNOM were inspired by the successes of STM, emulating the evanescent coupling character. Possibly the closest equivalent, albeit somewhat exotic, is the observation of photon tunneling through a gap filled with liquid metal.[22] Illumination by total internal reflection and pick up by a near-field probe that frustrates the evansecent fields shares similar evanescent field features with the STM.[23,24] In the late 1990s, a number of general and exact descriptions of SNOM were proposed, which arrive at formulas that closely resemble that of Bardeen.[25] Remarkably, no explicit assumption of weak coupling between sample and tip is necessary in their derivation. In principle, therefore, these formulas do also describe the operation of SNOMs—aperture-based or apertureless—that do not operate in the weak coupling regime.[26]

In the present report, we outline an approach to an analytic theory for recordable SNOM signals. The correlation between the general expressions for the electronic tunneling matrix elements and the optical reciprocity relations is rooted in the intimate relations between the Schrödinger equation and the Maxwell–Helmholtz equation,[27,28] which are the respective wave equations for the electron and photon. This suggests the possibility of picking up the idea of Tersoff and Hamann of a point-like probe tip for SNOM, as well. We show that it is possible to express recordable signals as an integral of the probing tip volume. Consequently, for apertureless or scattering-type SNOM—which are indeed point-like at the wavelength scale—an analytical, closed-form expression is obtained for the measured signals in SNOM that is analogous to the Tersoff–Hamann results. We demonstrate the utility of this framework in discussing how different forms of apertureless SNOM may be used to map local electric field components and how well these may be related to the bare sample near-fields.

RESULTS AND DISCUSSION

Bardeen's formula $M_{\mu\nu} \propto \int d\mathbf{S}\cdot(\psi_\mu^*\nabla\psi_\nu - \psi_\nu\nabla\psi_\mu^*)$ describes the flow of charge (or equivalently probability density) across a fictitious plane inserted in the gap between probe tip and sample. An analogon for SNOM has been derived earlier by Carminati, Greffet, and coworkers, who used reciprocity theory in their approach.[29]

Reciprocity describes the relation between two scenarios (1,2) under reciprocal illumination. Figure 1 displays a typical application for SNOM: in scenario 1, only the tip is present, and in scenario 2, both tip and sample are present. The tip can thus be defined and characterized (in scenario 1) without reference to any sample. This allows unravelling sample properties from the unknown signal generated by the sample being probed (in scenario 2).

Inside the volume V that contains the tip, the distribution of materials is identical in both scenarios; outside it may differ. The surface δV of this volume is presumed to be located entirely in vacuum, which causes $\nabla\mathbf{E}$ to vanish exactly. For point-like current sources, $\mathbf{j}_{1,2}^{(sou)} = \mathbf{I}_{1,2}\delta(\mathbf{r} - \mathbf{r}_{a,b})$, we write the reciprocity theorem as[30]

$$\frac{1}{i\omega\mu_0}\oint_{\delta V} dS\hat{\mathbf{n}}_i(\mathbf{E}_{1j}\partial_i\mathbf{E}_{2j} - \mathbf{E}_{2j}\partial_i\mathbf{E}_{1j}) = \mathbf{E}_1\cdot\mathbf{I}_2|_{\mathbf{r}_b} - \mathbf{E}_2\cdot\mathbf{I}_1|_{\mathbf{r}_a} \quad (1)$$

Formally, this integral is the equivalent of Bardeen's expression for a matrix element of the tunneling current. Bardeen's formula is an approximation for scalar (evanescent) wave functions solving the Schrödinger equation. Equation 1 solves the Maxwell equations exactly for vectorial fields, provided the materials inside the integration volume are nonmagnetic and have symmetric dielectric tensors.

The great advantages of eq 1 are the terms on the right-hand side. The currents are set parallel to the polarizations of the exciting ($\mathbf{I}_2$) and the detected ($\mathbf{I}_1$) radiation.[31] The electric signal measured in a given experiment is the term $\mathbf{E}_2\cdot\mathbf{I}_1$. The term $\mathbf{E}_1\cdot\mathbf{I}_2$ is an undesired background term that needs careful attention. In many cases, it is actually eliminated, for example, if $\mathbf{r}_b$ is outside of V, that is, in a transmission type of experiment. The same term also vanishes if $\mathbf{E}_1\perp\mathbf{I}_2$, which is the basis of the so-called cross-polarization scheme.[32]

To apply the reciprocity theorem eq 1 to SNOM, it is advantageous to choose a half-space confined by a plane parallel to the xy plane as integration volume (Figure 1). On the upper boundary, the surface integral vanishes under the Sommerfeld radiation condition. The remaining integral surface, the evaluation plane, allows for a successful treatment of the most general case in Fourier space.

In close analogy with experiment, the tip is chosen vertically aligned and the evaluation plane in the tip–sample gap. We proceed with computing the fields scattered by the tip alone $\mathbf{T} := \mathbf{E}_1|_{z_e}$ and the whole tip–sample system $\mathbf{S} := \mathbf{E}_2|_{z_e}$ on the evaluation plane. This is conveniently accomplished with an angular spectrum representation (see Methods section). Together with the volume equivalent representation[33] for the tip field, the exact expression for the measurable SNOM

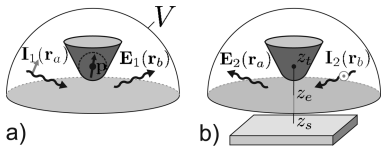

Figure 1. Two reciprocal scenarios. (a) In scenario 1, a source $\mathbf{I}_1$ at position $\mathbf{r}_a$ emits radiation, which is scattered by the tip and detected at position $\mathbf{r}_b$. (b) In the reciprocal scenario 2, an additional sample is present, whose surface right below the probe tip is at height z_s. Source and detector have exchanged their respective roles. A virtual evaluation plane is considered at height z_e in the gap between tip and sample.

signal (eq 1) becomes a comparatively simple term as an integral over the scattering tip volume

$$\mathbf{E}_2\cdot\mathbf{I}_1|_{\mathbf{r}_a} = \mathbf{E}_1\cdot\mathbf{I}_2|_{\mathbf{r}_b} - i\omega\int \mathrm{d}^3\mathbf{r}\mathbf{T}(\mathbf{r})\underline{\underline{\Delta\varepsilon}}(\mathbf{r})\mathbf{S}^+(\mathbf{r}) \quad (2)$$

Such integrals over small tip volumes are easily manageable with modern numerical Maxwell solvers. One may consider eq 2 as a fall-back option for delicate cases, or if specifically crafted probe tips deviated significantly from the point-like dipole model, which is considered next.

$\mathbf{S}^+(\mathbf{r}_t)$ should not be confused with the actual field $\mathbf{S}(\mathbf{r}_t)$ of the tip–sample system at the location of the tip in scenario 1. Instead, it denotes those field components that exist in the evaluation plane and travel up toward the tip, as displayed in angular spectrum representation.

Point-like Tip Model. In the form of eq 2, reciprocity theory is fully general, applicable to both aperture-based and apertureless versions of SNOM. We now ask what algebraic simplification and intuitive understanding can be gained if we restrict ourselves to point-like tips in the apertureless case? Nanoscopic probe tips, in the spirit of the dipole tip model,[34] are often treated as a point-like dipolar moment $\mathbf{p}(\mathbf{r}_t) = V_t\mathbf{T}(\mathbf{r}_t)\underline{\underline{\Delta\varepsilon}}(\mathbf{r}_t)$. This replacement turns eq 2 into the central result of this report, the simple scalar relation for the measured signal

$$\mathbf{E}_2\cdot\mathbf{I}_1|_{\mathbf{r}_a} = \mathbf{E}_1\cdot\mathbf{I}_2|_{\mathbf{r}_b} - i\omega\mathbf{p}(\mathbf{r}_t)\cdot\mathbf{S}^+(\mathbf{r}_t) \quad (3)$$

It is the equivalent of the Tersoff–Hamann formula $I \propto D_t(E_F)|\psi_\nu(\mathbf{r}_t)|^2$ for the tunneling current in STM. There, the measured signal is proportional to the square modulus of the sample wave function $|\psi_\nu(\mathbf{r}_t)|^2$ at the location of the tip, multiplied with the density of states D_t of the tip. In close analogy, the detected electric field is proportional to the field $\mathbf{S}^+(\mathbf{r}_t)$ at the tip position, projected by the inner product on the dipole moment $\mathbf{p}$ of the tip. One difference between STM and aSNOM is noteworthy: whereas $|\psi_\nu(\mathbf{r}_t)|^2$ is a property of the bare sample, $\mathbf{S}^+$ describes the fully coupled tip–sample system. Therefore, in the following, we discuss how the field $\mathbf{S}^+$ may be related to the unperturbed sample near-field $\mathbf{S}^{(\mathrm{unp})}$ in the absence of any probe tip.

Evaluation of the System Response. To evaluate the components of the system field $\mathbf{S}$ at the evaluation plane which travel upward, we adopt a Born series treatment of the tip–sample interaction.[35] Diagrammatically, the propagator of the coupled tip–sample system is represented by

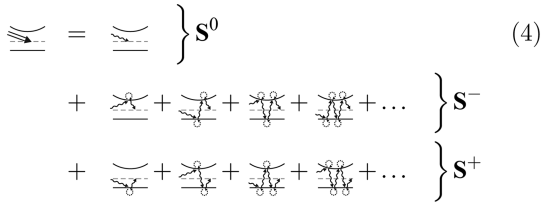

(4)

where the evaluation plane is indicated by the dotted horizontal line and sample and tip interfaces by a solid straight and curved line, respectively. Wiggly arrows represent the well-known vacuum propagator, and dotted arrows are self-depolarizations of the tip or sample

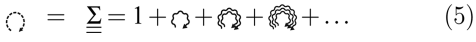

(5)

containing all orders of interactions of the sample or tip with itself.

We immediately see that all components traveling upward are scattered from the sample to the evaluation plane. The total field incident on the sample, however, is influenced by the near-field probe. The direct contribution $\mathbf{S}^0$ of the source $\mathbf{I}_2$ may be part of $\mathbf{S}^-$ or $\mathbf{S}^+$, depending on whether its location $\mathbf{r}_b$ is above or below the evaluation plane.

We abbreviate the consecutive action of a propagator and polarization by $\underline{\underline{\Gamma}}$ (see Methods section). We further introduce the interaction tensors

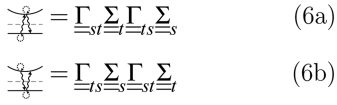

$$\underline{\underline{\Theta}}_{ss} = \underline{\underline{\Gamma}}_{sl}\underline{\underline{\Sigma}}_l\underline{\underline{\Gamma}}_{ts}\underline{\underline{\Sigma}}_s \quad (6a)$$

$$\underline{\underline{\Theta}}_{tt} = \underline{\underline{\Gamma}}_{ts}\underline{\underline{\Sigma}}_s\underline{\underline{\Gamma}}_{sl}\underline{\underline{\Sigma}}_l \quad (6b)$$

which describe one round trip action from the sample to the tip and back onto the sample itself or *vice versa*.

Algebraically, we can rewrite the upward traveling part of $\mathbf{S}$ according to eq 4 in two different versions as

$$\begin{aligned}\mathbf{S}^+ &= (\underline{\underline{\Gamma}}_{es}\underline{\underline{\Sigma}}_s)(1-\underline{\underline{\Theta}}_{ss})^{-1}(\mathbf{E}_s^{\mathrm{in}} + \underline{\underline{\Gamma}}_{st}\underline{\underline{\Sigma}}_t\mathbf{E}_t^{\mathrm{in}}) \\ &= \underline{\underline{\Gamma}}_{es}\underline{\underline{\Sigma}}_s\mathbf{E}_s^{\mathrm{in}}\end{aligned} \quad (7a)$$

$$+(\underline{\underline{\Gamma}}_{es}\underline{\underline{\Sigma}}_s\underline{\underline{\Gamma}}_{st}\underline{\underline{\Sigma}}_t)(1-\underline{\underline{\Theta}}_{tt})^{-1}\times(\underline{\underline{\Gamma}}_{ts}\underline{\underline{\Sigma}}_s\mathbf{E}_s^{\mathrm{in}} + \mathbf{E}_t^{\mathrm{in}}) \quad (7b)$$

depending on whether the view focuses on the tip (7b) or the sample (7a).

In the Born series picture, the desired measurable signal is thus generated in three steps. First, the incident radiation excites the tip and sample directly, and first-order scattering from one of them—say the sample—may be viewed as a coherent additional excitation of the other: $(\underline{\underline{\Gamma}}_{ts}\underline{\underline{\Sigma}}_s\mathbf{E}_s^{\mathrm{in}} + \mathbf{E}_t^{\mathrm{in}})$. Second, is an infinite series of interactions, whose terms can be summed up as a geometric sum: $(1-\underline{\underline{\Theta}}_{tt})^{-1}$. The third and last term contains $(\underline{\underline{\Gamma}}_{es}\underline{\underline{\Sigma}}_s)$, that is, the final scattering *via* the sample to the evaluation plane.

The interaction term $\underline{\underline{\Theta}}_{tt}$ is crucial for the validity of the Born series approach. The expansion can only sensibly be employed, if it converges, that is, if $\|\underline{\underline{\Theta}}_{tt}\| < 1$ in the sense of an operator norm. If the tip may be considered point-like, $\underline{\underline{\Theta}}_{tt}$ can be represented by a simple matrix, facilitating a direct criterion for when the Born series may be terminated after a suitable low order.

At this point, a cautious note regarding direct scattering from the tip to the detector may be in order. It is one of the major sources of undesired background, as it carries no information about the sample.

Any measurable signal that stems directly from the tip is due either to $\mathbf{S}^0 \in \mathbf{S}^+$, if the source $\mathbf{I}_2$ at $\mathbf{r}_b$ is located below the evaluation plane, or due to the term $(\mathbf{E}_1 \cdot \mathbf{I}_2)$, if $\mathbf{r}_b$ is above the evaluation plane, inside the integration volume. Thus, this parasitic background signal cannot generally be assumed to vanish, unless special care is taken to ensure exactly normal field vectors, $\mathbf{E}_1 \perp \mathbf{I}_2$,[36] or this signal is suppressed by modulation/demodulation techniques to a level below the detector noise floor.

We may terminate the Born series after an appropriate order, for example, in the case of a vanishingly small contribution from the tip (*i.e.*, $\underline{\underline{\alpha}}_t \to 0$, $\underline{\underline{\Gamma}}_{st} \to 0$, $\underline{\underline{\Sigma}}_t \to 1$). In that case, we find as the lowest order contributions to the measurable signal $\mathbf{S}^+$ the bare sample field and the first and second order terms

$$\mathbf{S}^{(unp)} = \quad = \underline{\underline{\Gamma}}_{es} \underline{\underline{\Sigma}}_s \mathbf{E}_s^{in} \tag{8a}$$

$$\mathbf{S}^{(1t)} = \quad = \underline{\underline{\Gamma}}_{es} \underline{\underline{\Sigma}}_s \underline{\underline{\Gamma}}_{st} \underline{\underline{\Sigma}}_t \mathbf{E}_t^{in} \tag{8b}$$

$$\mathbf{S}^{(2s)} = \quad = \underline{\underline{\Gamma}}_{es} \underline{\underline{\Sigma}}_s \underline{\underline{\Gamma}}_{st} \underline{\underline{\Sigma}}_t \underline{\underline{\Gamma}}_{ts} \underline{\underline{\Sigma}}_s \mathbf{E}_s^{in}$$

$$= \underline{\underline{\Theta}}_{tt} \mathbf{S}^{(unp)}(\mathbf{r}_t) \tag{8c}$$

In virtually all implementations of aSNOM, a modulation/demodulation scheme is employed. By oscillating the tip above the sample, $\mathbf{r}_t$ varies periodically in time with a frequency Ω. With the evaluation point $\mathbf{r}_t$ moving, the contributions to the measured signal $\mathbf{S}^+(\mathbf{r}_t(t))$ vary. Importantly, this alters $\mathbf{E}_t^{in}$, $\underline{\underline{\Gamma}}_{st}$, and $\underline{\underline{\Gamma}}_{ts}$ and hence all contributions to $\mathbf{S}^+$. After demodulating the measured signal at the fundamental Ω, one still measures considerable parasitic background signal due to $\mathbf{S}^0$ or $\mathbf{E}_1 \cdot \mathbf{I}_2$. Only by demodulation at the second or higher overtone of Ω can these (with some experimental care[37,38]) be sufficiently suppressed. To lowest order, the recorded signal is thus

$$\mathbf{E}_2 \cdot \mathbf{I}_1|_{\mathbf{r}_a} \approx i\omega \mathbf{p}(\mathbf{r}_t)(\mathbf{S}^{(unp)} + \mathbf{S}^{(1t)} + \mathbf{S}^{(2s)}) \tag{9}$$

which confirms the long-established experimental approach.[39]

With the field $\mathbf{S}^+$ of the tip−sample system known, we apply eq 3 to obtain the signal in typically employed experimental schemes for aSNOM. These are commonly classified by polarization configurations of the exciting and scattered radiation at the current sources. By suitably aligned, symmetric optics, one can ensure that the radiation has the same polarization at the center of the tip as at the source. As a demonstration, we choose a sample represented by a set of scattering points in vacuum. Already in this simple model, we can quantitatively compare signal contributions from different terms of the Born series (eq 7a) and learn which terms might contribute to the signal in the general case. From the analytic relation of each term to the unperturbed field, measured signals on unknown samples are intuitively interpretable.

Coupled-Dipole Model. The coupled-dipole model considers situations where the radiation at the tip from both $\mathbf{I}_1$ and $\mathbf{I}_2$ is parallel polarized. Both sources are assumed to be located at the same location $\mathbf{r}_a = \mathbf{r}_b$ inside the integration volume V. With additional assumptions regarding the reflection of the incident radiation at the sample interface[40−42] and the actual shape of an elongated tip, it is possible to approach a quantitative description. For situations where the probe tip is located above a flat, featureless substrate surface, the interaction of the tip with the surface is analytically described by the quasi-static coupled-dipole model, whose most sophisticated version was given by Cvitkovic *et al.*[43] For a point-like tip of polarizability α, the field scattered by the whole tip−sample system upon illumination with vertically polarized light is found proportional to

$$\mathbf{E}^{(sca)} \propto (1 + r_p)\alpha \left(1 - \frac{1}{16\pi R^3}\beta\alpha\right)^{-1} \times (r_p \mathbf{E}_s^{in} + \mathbf{E}_t^{in}) \tag{10}$$

where α is the polarizability of the tip, β and r_p the quasi-static and Fresnel refletion coefficients of the sample surface, respectively, and R is the height of the tip above the surface. An equivalent expression is found for the case of horizontally polarized radiation.

We recognize the great similarity to eq 7b . In eq 10, the contributions due to $\mathbf{S}^0$ and $\mathbf{E}_1 \cdot \mathbf{I}_2|_{\mathbf{r}_b}$ are not considered, as they are filtered out from the measured signal by demodulation, as discussed above. Both relations contain the full Born series of interactions, which allows extracting information about the material constants of the sample immediately underneath the tip. As no termination of a Born series is necessary, in this case, any probing tip may be used, regardless of the strength of its influence on the sample, as long as the signal remains measurable.

An advantage of eq 7b for future investigations is the possibility to extract more detailed information regarding the experimental conditions, such as the size of the lateral area over which the tip−sample interaction effectively averages, or how exactly the signal evolves as the tip moves laterally over a material contrast boundary or some topography changes, *etc.* For extended analysis of the influence of finite sized tips, eq 7 can be used in conjunction with eq 2 instead of eq 3 for point-like tips.

Cross-Polarized aSNOM. In the cross-polarized aSNOM configuration, the current source $\mathbf{I}_1$ in scenario 1 and the scattered field $\mathbf{E}_1(\mathbf{r}_a)$ are both p-polarized. If $\mathbf{I}_2$ is s-polarized (*i.e.*, $\mathbf{E}_1 \cdot \mathbf{I}_2 = 0$), then according to eq 3, the recorded signal simplifies to

$$\mathbf{E}_2 \cdot \mathbf{I}_1|_{\mathbf{r}_a} = -i\omega \mathbf{p}(\mathbf{r}_t) \cdot \mathbf{S}^+(\mathbf{r}_t) \tag{11}$$

regardless of the location of $\mathbf{r}_b$. We assume the tip is isotropic in the *xy* plane and mainly polarizable along

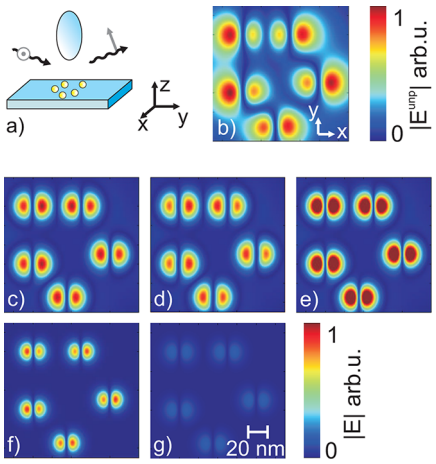

Figure 2. Simulation of signal components in cross-polarized aSNOM at λ = 1064 for the special case of a point-like tip and sample. (a) Sketch of the aSNOM configuration. A set of point-like dipoles representing spherical gold colloids is scanned by an anisotropic point-like tip, representing a silicon ellipsoid. Displayed are the *z*-components of (b) the unperturbed sample field $S^{(unp)}$ in the absence of any probe tip, compared to (c) the full Born series signal S^{+}, (d) the approximated signal, which is the coherent sum of (e) $S^{(unp)}$, (f) $S^{(1t)}$, and (g) $S^{(2s)}$, deconvoluted at the second overtone of the tip oscillation frequency. Each colloid responds with two lobes of opposite optical phase.

the *z*-axis. Choosing a grazing incidence excitation of the tip, its dipole **p** in scenario 1 is mainly vertically polarized. The measurement is thus sensitive mainly to the *z*-component of the field $\mathbf{S}^{+}$ of the tip−sample system in scenario 2. It is not clear at this point, though, what the disturbance due to the presence of the tip is. To this end, we relate $\mathbf{S}^{+}$ to the field due to an unperturbed sample $\mathbf{S}^{(unp)}$ in the absence of any probe tip.

We place the evaluation plane infinitesimally below the tip position. Under the assumption of a strongly anisotropically polarizable tip ($\underline{\alpha}_{tz} \gg \underline{\alpha}_{tx,y}$), the contribution $\mathbf{S}^{(1t)}$ to the signal becomes negligible, as the field $\mathbf{E}_t^{in}$ incident at the tip induces hardly any polarization. The Born series is dominated by $\mathbf{S}^{(unp)}$ and $\mathbf{S}^{(2s)}$ (see also Figure 2).

The measured signal is thus proprtional to $\mathbf{S}^{+} \approx (1 + \underline{\Theta}_{tt})\mathbf{S}^{(unp)}(\mathbf{r}_t)$. The interaction tensor $\underline{\Theta}_{tt}$ involves multiple three-dimensional convolutions; its exact nature is an intricate function of sample and tip geometry and will have to be subject to further detailed investigations.[44] For weak tips, $\underline{\Theta}_{tt} \ll 1$, the measured signal is proportional to the unperturbed field, convoluted with a lock-in demodulation effect.

Deconvoluting the signal at an overtone of the tip oscillation adds an additional spatial decay in the measured signal (compare Figure 2b,e). In the limit of infinitesimally small tip oscillation amplitudes, the signal recorded at the *n*th overtone is proportional to the $\partial^n/\partial z^n$ derivative of the field.[45] The recorded $\mathbf{S}^{+}$ image appears spatially sharpened relative to the unperturbed field image $\mathbf{S}^{(unp)}$. This is particularly prominent if both objects and tips are point-like. Also at the edge of sample structures, one may observe in cross-polarized aSNOM a more abrupt signal change than is actually present in $\mathbf{S}^{(unp)}$. Above extended sample regions, which vary smoothly on the scale of the tip size and exhibit slowly varying fields, the spatial contrast enhancement mentioned above is less pronounced.

These considerations are illustrated in Figure 2. Contrasting Figure 2c and Figure 2d affirms that the full Born series is well represented by the first-order approximation eq 9, which in turn is dominated by $\mathbf{S}^{(unp)}$ and $\mathbf{S}^{(2s)}$ (Figure 2f). The strongly *z*-polarizable tips conveniently used in cross-polarized aSNOM usually make the contribution $\mathbf{S}^{(1t)}$ to the full signal much weaker (Figure 2e). This analysis confirms that images obtained with cross-polarized aSNOM are good linear representations of the unperturbed bare sample fields. This is in agreement with the empirical finding that aSNOM in cross-polarization produces near-field optical maps that are very well reproduced by simulated near-field images of the bare substrate in the absence of any probing tip.[46−50]

Horizontal Component Mapping aSNOM. Recently, Hillenbrand *et al.* introduced another aSNOM configuration to measure horizontal electric fields.[51] The approach is somewhat similar to the coupled-dipole scenario, in that both incident and analyzed radiation have the same polarization. However, in the present case, they are s-polarized, which for very weakly s-polarizable probe tips generates an intricate interplay between the sample and the tip that is necessarily vectorial in nature.

Experimentally, two variations have been demonstrated. In transmission geometry, $\mathbf{r}_b$ is below the evaluation plane and eq 3 takes the form of eq 11 but includes an upward-propagating direct excitation $\mathbf{S}^0 \in \mathbf{S}^{+}$. In back-reflection geometry,[52] $\mathbf{r}_a = \mathbf{r}_b$ are both inside the integration volume, giving the measurable signal the form the full eq 3 . Here, the direct illumination does not contribute because $\mathbf{S}^0 \in \mathbf{S}^{-}$.

We may again assume the experimentally relevant case of a point-like tip that is mostly polarizable in the vertical direction, $\underline{\alpha}_{tz} \gg \underline{\alpha}_{tx,y} > 0$, but it must not be completely unpolarizable in the horizontal direction. Otherwise, the s-polarized dipole component $\mathbf{p}(\mathbf{r}_t)$ picked up at the location of the tip would vanish, and no measurable signal could be recorded.

In Figure 3, simulated near-field images showing the individual contributions to the signal are displayed. Except for projecting out the *x* component, the simulations were performed with parameters identical to the cross-polarized configuration of Figure 2 . Note that whereas Figure 2c-g displays a common color scale, as does Figure 3c-g, these color scales differ between these two cases by about 1 order of magnitude. Mainly due to the assumed stronger vertical polarizability of the probe tip, the recordable signals are stronger in the cross-polarized case.

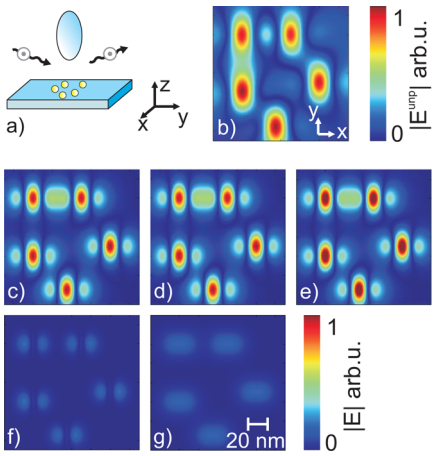

Figure 3. Simulation of signal components obtained with horizontal component mapping aSNOM. (a) Sketch of the aSNOM configuration. Except for projecting out the s-polarized component, the simulations were performed with parameters identical to the cross-polarized configuration of Figure 2 . Displayed are the *x* components of (b) the unperturbed sample field $S^{(unp)}$ in the absence of any probe tip, and (c) the full Born series signal S^{+}, (d) the approximated signal, which is the coherent sum of (e) $S^{(unp)}$, (f) $S^{(1t)}$, and (g) $S^{(2s)}$, deconvoluted at the second overtone of the tip oscillation frequency. The response of each colloid is dominated by a central lobe, except for (f), where this lobe is symmetry-forbidden. For a single colloid, all terms are symmetric in amplitude and phase to a vertical axis through the center of the colloid. We discard the background term $E_1 \cdot I_2|_{r_b}$ of eq 3 .

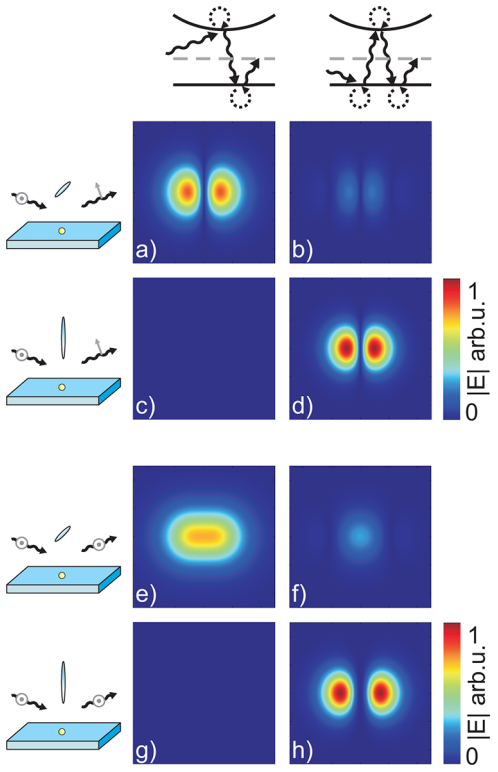

Figure 4. Comparison of the first-order contributions to the field S^{+} picked up by differently polarizable tips in different aSNOM configurations. All images show a point-like dipole representing a spherical gold colloid of 10 diameter, scanned by a point-like tip polarizable exclusively in *x*-direction (a,b,e,f) or in *z*-direction (c,d,g,h) by the same magnitude. The excitation is always assumed to be s-polarized radiation of 1064 wavelength. (a−d) Cross-polarized aSNOM images, (e−h) horizontal component mapping aSNOM images. The left row (a,c,e,g) shows the $S^{(1t)}$ contribution, the right row (b,d,f,h) shows $S^{(2s)}$.

The comparison of Figure 3c,d shows that, as in the case of cross-polarized aSNOM, the full Born series is well approximated by the two lowest relevant orders, following eq 9. Evidently, with the simulation parameters chosen in Figure 3, the approximated field is dominated by the unperturbed field. For stronger interacting tips, also the higher order terms $\mathbf{S}^{(1t)}$ and $\mathbf{S}^{(2s)}$ will contribute to the signal significantly.

Both terms $\mathbf{S}^{(1t)}$ and $\mathbf{S}^{(2s)}$ can be of the same order and contribute coherently to the measured signal (Figure 3e,f) in very different forms. To explore this situation further, we compare numerical aSNOM images generated with exclusively *z*- or *x*-polarizable tips in Figure 4 . For both cross-polarized and horizontal component mapping, aSNOM *z*-polarizability exclusively contributes to $\mathbf{S}^{(2s)}$ (Figure 4d,h). The s-polarized incident light cannot excite the tip, and $\mathbf{S}^{(1t)}$ vanishes in these cases (Figure 4c,g). Horizontal polarizability predominantly contributes to the signal term $\mathbf{S}^{(1t)}$, excited by light incident on the tip (Figure 4a,e). However, the $\mathbf{S}^{(2s)}$ components are not zero in these cases (Figure 4b,f). For probe tips predominantly polarizable in *x*-direction, $\mathbf{S}^{(2s)}$ can be suppressed in favor of $\mathbf{S}^{(1t)}$.[53]

Note that the aSNOM image presented in Figure 4h only appears to be of dipolar character. Both lobes are symmetric in amplitude and phase, and the central node line occurs for symmetry reasons. According to eq 8c, it represents the unperturbed field $\mathbf{S}^{(unp)}$, convoluted with $\underline{\Theta}_{tt}$. In the *yz* symmetry plane of an excited *x*-dipole, however, no coupling to a *z*-polarizable tip is possible and $\underline{\Theta}_{tt}$ vanishes. The signal due to $\mathbf{S}^{(1t)}$ (Figure 4e) is favorable in this respect. According to eq 8b, however, this signal does not represent the unperturbed response of the sample to the field $\mathbf{E}_s^{in}$ directly incident on the sample. Rather it represents a different sample response to an excitation emitted indirectly by the tip, $\tilde{\mathbf{E}}_s^{in} = \underline{\Gamma}_{st} \underline{\Sigma}_t \mathbf{E}_t^{in}$.

CONCLUSIONS

We have provided a general and exact framework for the measurable signals in scanning near-field optical microscopy. The starting point is a form of reciprocity theory appropriate for dissipative, nonmagnetic, reciprocal tips. (In passing, we note the possibility of an analogous theory for transparent, nonmagnetic, but nonreciprocal tips, which bears great similarity with energy conservation theorems.) As was already reported earlier by Carminati, Greffet, and co-workers,[54] only the upward traveling components of the coupled tip−sample system contribute to any measurable signal. With the goal of an intuitive formulation that allows immediate conclusions about qualitative aspects of

SNOM, our variant of the theory is expressed as an integral over the probing tip's volume (eq 2). It can be conveniently reduced to the point-like tip case (eq 3). This latter formulation constitutes an analogue to the formula of Tersoff and Hamann for the analysis of scanning tunneling microscopy signals obtained with point-like electrodes.

The analysis of the upward traveling field components is achieved in a Born series framework. A criterion for the applicability of the Born series is given. We discuss a number of typical experimental situations: the coupled-dipole model, the cross-polarization scheme for mapping out-of-plane field components, and horizontal component mapping of electric field components. All of them are found to be amenable to analysis with the model presented here, which indicates its utility also for future developments in scanning near-field microscopy.

METHODS

Reciprocity Theory. To motivate the application of reciprocity theory, it is convenient to draw attention to an often unnoted intimate relation between reciprocity and energy conservation. Indeed, at first sight, the flow of energy across an interface separating a sample from a near-field probe tip might seem like an opportune candidate to establish an optical analogue to the probability flow in Bardeen's case. The flow of energy is represented by the Poynting field $\mathbf{S} = \mathbf{E} \times \mathbf{H}$, and the associated theorem for optical energy conservation is well-known.[55] Its close relative, the reciprocity theorem, contains terms of similar shape ($\mathbf{E}_2 \times \mathbf{H}_1 - \mathbf{E}_1 \times \mathbf{H}_2$). It constitutes a relation between the fields in two scenarios 1 and 2 under different illumination conditions.[56]

To treat energy conservation and reciprocity in the same formalism, we rewrite the Poynting vector as $2\mathbf{S} = (\mathbf{E}_2 \times \mathbf{H}_1 + \mathbf{E}_1 \times \mathbf{H}_2)$ with both scenarios being identical. In the following, we consider generalized terms ($\mathbf{E}_2 \times \mathbf{H}_1 + \zeta\mathbf{E}_1 \times \mathbf{H}_2$). This puts reciprocity theory on par with energy conservation. The sign factor $\zeta = \pm 1$ automatically tracks both energy and reciprocity theory, and an explicit choice is made after it has become evident which theorem is best suited. We start from the Maxwell equations in SI units

$$\nabla\mathbf{D} = \rho \tag{12a}$$

$$\nabla \times \mathbf{E} = -\dot{\mathbf{B}} \tag{12b}$$

$$\nabla\mathbf{B} = 0 \tag{12c}$$

$$\nabla \times \mathbf{H} = \dot{\mathbf{D}} + \mathbf{j} \tag{12d}$$

with the constitutive equations

$$\mathbf{D} = \underline{\varepsilon}\mathbf{E} \tag{13a}$$

$$\mathbf{B} = \underline{\mu}\mathbf{H} \tag{13b}$$

$$\mathbf{j} = \underline{\sigma}\mathbf{E} \tag{13c}$$

All material properties are described by unit bearing quantities; that is, they are *not* measured relative to the vacuum values ε_0 and μ_0; $\underline{\varepsilon}$ and $\underline{\mu}$ are the electric and magnetic permittivity, respectively, and $\underline{\sigma}$ the conductivity. By multiplying $\mathbf{H}\cdot$ with eq 12b and $\mathbf{E}\cdot$ with eq 12d and adding appropriately, one obtains

$$-\nabla(\mathbf{E}_2 \times \mathbf{H}_1 + \zeta\mathbf{E}_1 \times \mathbf{H}_2) = \mathbf{H}_1\dot{\mathbf{B}}_2 + \zeta\mathbf{H}_2\dot{\mathbf{B}}_1 + \mathbf{E}_2\dot{\mathbf{D}}_1 + \zeta\mathbf{E}_1\dot{\mathbf{D}}_2 + \mathbf{E}_2\mathbf{j}_1 + \zeta\mathbf{E}_1\mathbf{j}_2 \tag{14}$$

Here the fields $\mathbf{E},\mathbf{D},\mathbf{H},\mathbf{B},\mathbf{j}$ are all real-valued functions of space and time. The indices 1 and 2 refer to the two different scenarios, as depicted in Figure 1. In both scenarios, a volume V is considered to enclose the scattering probing tip located at $\mathbf{r}_t$ with a hemisphere of infinite radius. The distribution of material scatterers inside the volume does not change, but the fields are generally very different. In scenario 1, a source $\mathbf{I}_1$ at position $\mathbf{r}_a$ emits radiation, giving rise to $\mathbf{E}_1$ at position $\mathbf{r}_b$. In the reciprocal scenario 2, an additional sample is present outside the integration volume. Source and detector have exchanged their places; source $\mathbf{I}_2$ at position $\mathbf{r}_b$ emits radiation, which leads to a field $\mathbf{E}_2$ at position $\mathbf{r}_a$.

The material operators $\underline{\varepsilon}, \underline{\mu}, \underline{\sigma}$ are local functions of space, describing causal responses in time, most easily represented as Kramers–Kronig compatible functions of frequency. This calls naturally for a complex-valued representation, which is carefully introduced by substituting $\mathbf{E} \rightarrow \mathscr{R}\mathbf{E} = (1/2)(\mathbf{E}+\bar{\mathbf{E}})$, *etc.* It is also most convenient for near-monochromatic scenarios,[57,58] such as those excited by narrow-band laser sources, in which all time-dependent phenomena vary with frequencies in a narrow band $\Delta\omega$ around a central frequency ω. As is well-known, in this case, product terms separate into two classes: fast terms, which oscillate (approximately) with $\exp(-2i\omega t)$, and slowly varying terms, which vary on frequency scales less than $\Delta\omega$. Thus, there are four possible equations, namely, the fast and slow terms in the energy ($\zeta = +1$) or reciprocity ($\zeta = -1$) theorem.

Here we concentrate on the exact monochromatic approximation. In this case, it is advantageous to split the current densities into source and scattering parts, $\mathbf{j} = \mathbf{j}^{(sou)} + \mathbf{j}^{(sca)}$, and to subsume the conductivity tensor for all scattering media in the dielectric permeability, $\tilde{\underline{\varepsilon}} = \underline{\varepsilon} - \underline{\sigma}/i\omega$. The slow terms of the energy conservation theorem are

$$\mathscr{R}\nabla(\overline{\mathbf{E}_2} \times \mathbf{H}_1 + \overline{\mathbf{E}_1} \times \mathbf{H}_2) = +\mathscr{R}(2i\omega)(\overline{\mathbf{E}_1}\tilde{\underline{\varepsilon}}^{AH}\mathbf{E}_2 + \overline{\mathbf{H}_2}\underline{\mu}^{AH}\mathbf{H}_1) - \mathscr{R}(\overline{\mathbf{E}_1}\cdot\mathbf{j}_2^{(sou)} + \overline{\mathbf{E}_2}\cdot\mathbf{j}_1^{(sou)}) \tag{15}$$

Conventionally, only the slow terms are regarded as relevant to optical measurements because the fast terms oscillate with frequencies $2\omega \gg$ THz and are orders of magnitude faster than what is detectable with currently available detectors. Curiously, though, the slow energy conservation terms correspond algebraically most closely to the fast terms of the reciprocity theorem

$$\mathscr{R}\nabla(\mathbf{E}_1 \times \mathbf{H}_2 - \mathbf{E}_2 \times \mathbf{H}_1) = +\mathscr{R}(2i\omega)(\mathbf{E}_1\tilde{\underline{\varepsilon}}^{AS}\mathbf{E}_2 + \mathbf{H}_2\underline{\mu}^{AS}\mathbf{H}_1) - \mathscr{R}(\mathbf{E}_1\cdot\mathbf{j}_2^{(sou)} - \mathbf{E}_2\cdot\mathbf{j}_1^{(sou)}) \tag{16}$$

Besides the great similarity between eqs 15 and 16, there are subtle, yet crucial, differences. Whereas we do make no assumptions about the symmetry of the material tensors, the first terms on the right-hand sides of the energy and reciprocity relation contain, respectively, only the anti-Hermitian and antisymmetric parts. If these terms do not vanish by symmetry, they can pose considerable numerical difficulties in further applications of the equations.

One may choose one or the other, depending on whether the material tensors are Hermitian or symmetric, respectively. (Note that this concerns only the inside of the hemispherical volume.) On the one hand, energy conservation may be successfully applied to magneto-optically active and other materials that break (local) time-reversal symmetry.[59] Reciprocity, on the other hand, usually facilitates dissipative media, which break (optical) energy conservation. These algebraic considerations hint at the underlying deeper symmetries that exist

between energy conservation, time-reversal symmetry, and reciprocity.

We assume a symmetric dielectric function $\underline{\tilde{\varepsilon}}^{AS} = 0$ and nonmagnetic materials. We integrate eq 16 over a volume containing the tip and use the Gauss theorem to transform it into the surface integral eq 1.

Angular Spectrum Representation. For evaluating eq 1, we represent both fields scattered by the tip and the whole system in the evaluation plane using angular spectrum representation. Angular spectrum representation is based on a two-dimensional Fourier transform of electric fields. The Helmholtz equation constitutes the out-of plane propagation constant $k_0^2 = \omega^2/c^2$. We distinguish between components traveling upward ($\xi = +1$) and downward ($\xi = -1$).

$$\mathbf{E}_i(\mathbf{r}) = \sum_{\xi=\pm 1} \frac{1}{2\pi} \iint \mathrm{d}^2\mathbf{k}_{\parallel}\, \mathbf{E}_i^{\xi}(\mathbf{k}_{\parallel}, z_0) \times \exp(\xi i k_z (r_z - z_0)) \exp(i\mathbf{k}_{\parallel}\mathbf{r}_{\parallel})$$

$$k_z = +\sqrt{k_0^2 - k_{\parallel}^2} \text{ for propagating modes}$$

$$k_z = +i\sqrt{k_{\parallel}^2 - k_0^2} \text{ for evanescent modes} \qquad (17)$$

The upward and downward traveling field components $\xi = \pm 1$ can be separated in Fourier space

$$\mathbf{E}(\mathbf{k}_{\parallel}, z) = \frac{1}{2\pi} \iint \mathrm{d}^2\mathbf{k}_{\parallel}\, \mathbf{E}(\mathbf{r}) \exp(-i\mathbf{k}_{\parallel}\mathbf{r}_{\parallel}) \qquad (18)$$

through the use of a projection operator

$$\mathbf{E}^{\xi}(\mathbf{k}_{\parallel}, z) = \frac{k_z - i\xi\partial_z}{2k_z} \mathbf{E}(\mathbf{k}_{\parallel}, z) \qquad (19)$$

Notice that this requires, besides the field in the evaluation plane, also its normal derivative. An alternative scheme might be more convenient for certain numerical implementations. If the derivative of the field in the transformation plane is not available, but the fields are known in two parallel planes close to each other, the projections can also be obtained as

$$\mathbf{E}^{\xi}(\mathbf{k}_{\parallel}, z) = \xi \frac{\mathbf{E}(\mathbf{k}_{\parallel}, z) - \mathbf{E}(\mathbf{k}_{\parallel}, z + \Delta z)\exp(-\xi i k_z \Delta z)}{2i\sin(k_z \Delta z)}$$

$$\times \exp(-\xi i \mathbf{k}_{\parallel}\mathbf{r}_{\parallel}) \qquad (20)$$

Once the fields are distinguished into their upward and downward traveling components, one can propagate them very easily from one plane to another:

$$\mathbf{E}^{\xi}(\mathbf{k}_{\parallel}, z) = \mathbf{E}^{\xi}(\mathbf{k}_{\parallel}, z_0)\exp(\xi i k_z (z - z_0)) \qquad (21)$$

Note that this propagation may only be applied inside of homogeneous media. In our case, fields are propagated through the gap between tip and sample.

Integration over the Evaluation Plane. In order to derive eq 2, we use the self-consistent scattered field expression for the tip field

$$\mathbf{T}_i(\mathbf{r}) = \frac{k_0^2}{\varepsilon_0} \int \mathrm{d}^3\mathbf{r}' \mathbf{T}_m(\mathbf{r}') \Delta\underline{\underline{\varepsilon}}_{mj}(\mathbf{r}') \times \left(1 + \frac{\nabla_j \nabla_i}{k_0^2}\right) \frac{e^{ik_0|\mathbf{r}-\mathbf{r}'|}}{|\mathbf{r}-\mathbf{r}'|} \qquad (22)$$

Here, $\Delta\underline{\underline{\varepsilon}}$ is the difference between the scatterer permittivity and the background medium. The integration volume covers only the finite tip volume, where $\Delta\underline{\underline{\varepsilon}}$ is nonzero. With the angular spectrum representation of the scalar Green function[60−62]

$$\frac{e^{ik_0|\mathbf{r}|}}{|\mathbf{r}|} = -\frac{i}{8\pi^2} \iint \mathrm{d}^2\tilde{\mathbf{k}}_{\parallel} \frac{1}{\tilde{k}_z} e_z^{-i\tilde{k}} r_z e^{i\tilde{\mathbf{k}}_{\parallel}\mathbf{r}_{\parallel}} \qquad (23)$$

one can substitute eq 22 for **T** and eq 17 for **S** in eq 1. After a few algebraic manipulations, eq 2 is obtained.

Green Functions. As is well-known, a single scattering event is mediated by the vacuum Green dyadic of the Helmholtz equation

$$\underline{\underline{G}}_{ij}^0(\mathbf{r}, \mathbf{r}') = -\left(1 + \frac{\nabla_j \nabla_i}{k_0^2}\right) \frac{\exp(ik_0|\mathbf{r}-\mathbf{r}'|)}{4\pi|\mathbf{r}-\mathbf{r}'|} \qquad (24)$$

We introduce the tensor $\underline{\underline{\Gamma}} = (k_0^2/\varepsilon_0)\underline{\underline{G}}^0\underline{\underline{\alpha}}$ to describe the consecutive action of polarizing a scatterer and propagating the scattered field to the target location. The polarizability is $\underline{\underline{\alpha}} = \int \mathrm{d}V \Delta\underline{\underline{\varepsilon}}$.

We abbreviate the fields after a single scattering event by

$$\mathbf{E}^{sca}(\mathbf{r}) = -\int \mathrm{d}^3\mathbf{r}' \underline{\underline{G}}^0(\mathbf{r}, \mathbf{r}') \Delta\underline{\underline{\varepsilon}}(\mathbf{r}') \mathbf{E}^{in}(\mathbf{r}') \qquad (25a)$$

$$= \underline{\underline{\Gamma}}\mathbf{E}^{in} \qquad (25b)$$

In this sense, the self-interaction of tip and sample (eq 5) can be written as

$$\underline{\underline{\Sigma}} = \sum_{n=0}^{\infty} \underline{\underline{\Gamma}}^n = (1 - \Gamma)^{-1} \qquad (26)$$

We write the upward traveling part of the sample-field according to eq 4 as

$$\mathbf{S}^{+} = (\underline{\underline{\Gamma}}_{es}\underline{\underline{\Sigma}}_{s}) \times (1 + \underline{\underline{\Theta}}_{ss} + \underline{\underline{\Theta}}_{ss}^2 + \ldots) \times (\mathbf{E}_s^{in} + \underline{\underline{\Gamma}}_{st}\underline{\underline{\Sigma}}_{t}\mathbf{E}_t^{in}) \qquad (27)$$

which we abbreviate as eq 7a.

Numerical Evaluation for Point-like Samples. In a typical experiment, one considers an excitation source at a certain location, which gives rise to a scattered field. At another location, one places a detector, which then measures the effect communicated from the source to the detector. In numerical simulations, this signal can be calculated straightforwardly with any variant of rigorous Maxwell equation solving method. Essentially, one computes in a single scenario the transmission of energy from the source to the detector.

Reciprocity theory uses a different approach to obtain this signal, which considers two reciprocal scenarios. It establishes relations between oscillating currents and resulting electric fields if one interchanges the locations where the currents are placed and where the fields are measured. For computing optical scattering signals, one considers in the first scenario the source currents that generate the exciting radiation as in an actual experiment. The resulting fields are evaluated at the location of the detector. In the second scenario, their places are interchanged. In this case, one considers currents in the place of the detector to excite scattered response fields at the location of the source. This may at first seem somewhat counterintuitive. By combining the two scenarios, however, it is possible to establish a relation that directly represents the experimentally measured signal.

To motivate further the application of reciprocity theory, we apply the field of the tip−sample system to the case of a sample consisting of point-like scatterers in vacuum. The scatterer polarizabilities represent spherical gold colloids of 10 nm diameter. The refractive index of gold at 1064 nm wavelength is taken from Johnson and Christy.[63] The tip−sample distance is 25 nm. The polarizability of the tip is assumed to be the same as a 10 nm diameter sphere of silicon for the in-plane components. We chose that value according to the data sheet of typical silicon tips employed in our experimental setup (ATEC-NC, Nano and More). In Figures 2 and 3, we chose the out-of plane component of the tip polarizability 10 times as large as the in-plane components. In Figure 4, the magnitude of dipolar moment is equal between individual tips $p_{xa,b} = p_{zc,d}$. The point sources $\mathbf{I}_{1,2}$ are collimated by optics inside the integration volume. The exact geometry of illumination and detection path is represented by the tensorial connection between source current $\mathbf{I}_{1,2}$ and incident field on tip and sample. In the simulation, we assume the illumination field to be a plane wave of same polarization as the sources, making this tensor a multiple of the unit operator. The angle of illumination is 70° from the surface normal. The (complex valued) measured signal at the second overtone of the tip oscillation frequency is proportional to

$$\mathbf{E}_2 \cdot \mathbf{I}_1|_{2\Omega} \propto \int_0^{2\pi/\Omega} \mathrm{d}t \mathbf{p}(\mathbf{r}_t(t)) \cdot \mathbf{S}^{+}(\mathbf{r}_t(t)) \cdot \exp(2i\Omega t) \qquad (28)$$

We plot the absolute value of the signal. The field incident on the tip in scenario 1 changes with the oscillating tip position. The dipolar

moment **p** changes with time, and also portions of **S** changing linearly with tip−sample distance contribute to the signal. This includes far-field scattering of a substrate−air interface.

The images are a demonstration of the Green function ansatz for discrete sample dipoles to show the Born series may be terminated after few orders. More sophisticated models for sample and tip can be easily applied using eq 2.

Conflict of Interest: The authors declare no competing financial interest.

REFERENCES AND NOTES

1. Lieber, C. M. Nanoscale Science and Technology: Building a Big Future from Small Things. *MRS Bull.* **2003**, *28*, 486–491.
2. Kelly, K. L.; Coronado, E.; Zhao, L. L.; Schatz, G. C. The Optical Properties of Metal Nanoparticles: The Influence of Size, Shape, and Dielectric Environment. *J. Phys. Chem. B* **2003**, *107*, 668–677.
3. Barnes, W. L.; Dereux, A.; Ebbesen, T. W. Surface Plasmon Subwavelength Optics. *Nature* **2003**, *424*, 824–830.
4. Rosi, N. L.; Mirkin, C. A. Nanostructures in Biodiagnostics. *Chem. Rev.* **2005**, *105*, 1547–1562.
5. Maier, S. A.; Atwater, H. A. Plasmonics: Localization and Guiding of Electromagnetic Energy in Metal/Dielectric Structures. *J. Appl. Phys.* **2005**, *98*, 011101.
6. Ozbay, E. Plasmonics: Merging Photonics and Electronics at Nanoscale Dimensions. *Science* **2006**, *311*, 189–193.
7. Jain, P. K.; Huang, X.; El-Sayed, I. H.; El-Sayed, M. A. Noble Metals on the Nanoscale: Optical and Photothermal Properties and Some Applications in Imaging, Sensing, Biology, and Medicine. *Acc. Chem. Res.* **2008**, *41*, 1578–1586.
8. Yoshida, M.; Lahann, J. Smart Nanomaterials. *ACS Nano* **2008**, *2*, 1101–1107.
9. Anker, J. N.; Hall, W. P.; Lyandres, O.; Shah, N. C.; Zhao, J.; Van Duyne, R. P. Biosensing with Plasmonic Nanosensors. *Nat. Mater.* **2008**, *7*, 442–453.
10. Halas, N. J. Plasmonics: An Emerging Field Fostered by Nano Letters. *Nano Lett.* **2010**, *10*, 3816–3822.
11. Vogelgesang, R.; Dmitriev, A. Real-Space Imaging of Nanoplasmonic Resonances. *Analyst* **2010**, *135*, 1175–1181.
12. Méndez, E.; Greffet, J.-J.; Carminati, R. On the Equivalence between the Illumination and Collection Modes of the Scanning Near-Field Optical Microscope. *Opt. Commun.* **1997**, *142*, 7–13.
13. Carney, P. S.; Schotland, J. C. Inverse Scattering for Near-Field Microscopy. *Appl. Phys. Lett.* **2000**, *77*, 2798–2800.
14. Carney, P. S.; Frazin, R. A.; Bozhevolnyi, S. I.; Volkov, V. S.; Boltasseva, A.; Schotland, J. C. Computational Lens for the Near Field. *Phys. Rev. Lett.* **2004**, *92*, 163903.
15. Kosobukin, V. Theory of Scanning Near-Field Magnetooptical Microscopy. *Tech. Phys.* **1998**, *43*, 824–829.
16. Taminiau, T. H.; Moerland, R. J.; Segerink, F. B.; Kuipers, L. K.; van Hulst, N. F. $\lambda/4$ Resonance of an Optical Monopole Antenna Probed by Single Molecule Fluorescence. *Nano Lett.* **2007**, *7*, 28–33.
17. Walford, J. N.; Porto, J.-A.; Carminati, R.; Greffet, J.-J. Theory of Near-Field Magneto-Optical Imaging. *J. Opt. Soc. Am. A* **2002**, *19*, 572–583.
18. Greffet, J.-J.; Carminati, R. Image Formation in Near-Field Optics. *Prog. Surf. Sci.* **1997**, *56*, 133–237.
19. Tersoff, J.; Hamann, D. R. Theory and Application for the Scanning Tunneling Microscope. *Phys. Rev. Lett.* **1983**, *50*, 1998–2001.
20. Tersoff, J.; Hamann, D. R. Theory of the Scanning Tunneling Microscope. *Phys. Rev. B* **1985**, *31*, 805–813.
21. Bardeen, J. Tunnelling from a Many-Particle Point of View. *Phys. Rev. Lett.* **1961**, *6*, 57–59.
22. Pohl, W. D. Near-Field Photon Tunneling Devices Using Liquid Metal. U.S. Patent 5619600, 1997.
23. Krenn, J.; Wolf, R.; Leitner, A.; Aussenegg, F. Near-Field Optical Imaging the Surface Plasmon Fields of Lithographically Designed Nanostructures. *Opt. Commun.* **1997**, *137*, 46–50.
24. Krenn, J.; Dereux, A.; Weeber, J.; Bourillot, E.; Lacroute, Y.; Goudonnet, J.; Schider, G.; Gotschy, W.; Leitner, A.; Aussenegg, F.; *et al.* Squeezing the Optical Near-Field Zone by Plasmon Coupling of Metallic Nanoparticles. *Phys. Rev. Lett.* **1999**, *82*, 2590–2593.
25. Carminati, R.; Sáenz, J. J. Scattering Theory of Bardeen's Formalism for Tunneling: New Approach to Near-Field Microscopy. *Phys. Rev. Lett.* **2000**, *84*, 5156–5159.
26. Knoll, B.; Keilmann, F. Enhanced Dielectric Contrast in Scattering-Type Scanning Near-Field Optical Microscopy. *Opt. Commun.* **2000**, *182*, 321–328.
27. De Raedt, H.; Lagendijk, A.; de Vries, P. Transverse Localization of Light. *Phys. Rev. Lett.* **1989**, *62*, 47–50.
28. Steuernagel, O. Equivalence between Focused Paraxial Beams and the Quantum Harmonic Oscillator. *Am. J. Phys.* **2005**, *73*, 625–629.
29. Carminati, R.; Sáenz, J. J.; Greffet, J.-J.; Nieto-Vesperinas, M. Reciprocity, Unitarity, and Time-Reversal Symmetry of the S Matrix of Fields Containing Evanescent Components. *Phys. Rev. A* **2000**, *62*, 012712.
30. Porto, J. A.; Carminati, R.; Greffet, J.-J. Theory of Electromagnetic Field Imaging and Spectroscopy in Scanning Near-Field Optical Microscopy. *J. Appl. Phys.* **2000**, *88*, 4845–4850.
31. Monteath, G. D. *Applications of the Electromagnetic Reciprocity Principle*; Pergamon Press: New York, 1973.
32. Esteban, R.; Vogelgesang, R.; Dorfmüller, J.; Dmitriev, A.; Rockstuhl, C.; Etrich, C.; Kern, K. Direct Near-Field Optical Imaging of Higher Order Plasmonic Resonances. *Nano Lett.* **2008**, *8*, 3155–3159.
33. Balanis, C. A. *Advanced Engineering Electromagnetics*; Wiley: New York, 1989.
34. Koglin, J.; Fischer, U. C.; Fuchs, H. Material Contrast in Scanning Near-Field Optical Microscopy at 1−10 nm Resolution. *Phys. Rev. B* **1997**, *55*, 7977–7984.
35. Sun, J.; Carney, P. S. Strong Tip Effects in Near-Field Scanning Optical Tomography. *J. Appl. Phys.* **2007**, *102*, 103103.
36. Esslinger, M.; Dorfmüller, J.; Khunsin, W.; Vogelgesang, R.; Kern, K. Background-Free Imaging of Plasmonic Structures with Cross-Polarized Apertureless Scanning Near-Field Optical Microscopy. *Rev. Sci. Instrum.* **2012**, *83*, 033704.
37. Vogelgesang, R.; Esteban, R.; Kern, K. Beyond Lock-in Analysis for Volumetric Imaging in Apertureless Scanning Near-Field Optical Microscopy. *J. Microsc.* **2008**, *229*, 365–370.
38. Esteban, R.; Vogelgesang, R.; Kern, K. Simulation of Optical Near and Far Fields of Dielectric Apertureless Scanning Probes. *Nanotechnology* **2006**, *17*, 475–482.
39. Hillenbrand, R.; Keilmann, F. Complex Optical Constants on a Subwavelength Scale. *Phys. Rev. Lett.* **2000**, *85*, 3029–3032.
40. Raschke, M. B.; Lienau, C. Apertureless Near-Field Optical Microscopy: Tip−Sample Coupling in Elastic Light Scattering. *Appl. Phys. Lett.* **2003**, *83*, 5089–5091.
41. Bek, A. Apertureless SNOM: A New Tool for Nano-Optics. Ph.D. Thesis, EPFL, 2004.
42. Renger, J.; Grafström, S.; Eng, L. M.; Hillenbrand, R. Resonant Light Scattering by Near-Field-Induced Phonon Polaritons. *Phys. Rev. B* **2005**, *71*, 075410.
43. Cvitkovic, A.; Ocelic, N.; Hillenbrand, R. Analytical Model for Quantitative Prediction of Material Contrasts in Scattering-Type Near-Field Optical Microscopy. *Opt. Express* **2007**, *15*, 8550–8565.
44. Deutsch, B.; Hillenbrand, R.; Novotny, L. Visualizing the Optical Interaction Tensor of a Gold Nanoparticle Pair. *Nano Lett.* **2010**, *10*, 652–656.
45. Walford, J. N.; Porto, J. A.; Carminati, R.; Greffet, J.-J.; Adam, P. M.; Hudlet, S.; Bijeon, J.-L.; Stashkevich, A.; Royer, P. Influence of Tip Modulation on Image Formation in Scanning Near-Field Optical Microscopy. *J. Appl. Phys.* **2001**, *89*, 5159–5169.
46. Zentgraf, T.; Dorfmüller, J.; Rockstuhl, C.; Etrich, C.; Vogelgesang, R.; Kern, K.; Pertsch, T.; Lederer, F.; Giessen, H. Amplitude- and Phase-Resolved Optical Near Fields of Split-Ring-Resonator-Based Metamaterials. *Opt. Lett.* **2008**, *33*, 848–850.

47. Dorfmüller, J.; Vogelgesang, R.; Weitz, R. T.; Rockstuhl, C.; Etrich, C.; Pertsch, T.; Lederer, F.; Kern, K. Fabry-Pérot Resonances in One-Dimensional Plasmonic Nanostructures. *Nano Lett.* **2009**, *9*, 2372–2377.
48. Dorfmüller, J.; Vogelgesang, R.; Khunsin, W.; Rockstuhl, C.; Etrich, C.; Kern, K. Plasmonic Nanowire Antennas: Experiment, Simulation, and Theory. *Nano Lett.* **2010**, *10*, 3596–3603.
49. Dorfmüller, J.; Dregely, D.; Esslinger, M.; Khunsin, W.; Vogelgesang, R.; Kern, K.; Giessen, H. Near-Field Dynamics of Optical Yagi-Uda Nanoantennas. *Nano Lett.* **2011**, *11*, 2819–2824.
50. Dregely, D.; Taubert, R.; Dorfmuller, J.; Vogelgesang, R.; Kern, K.; Giessen, H. 3D Optical Yagi-Uda Nanoantenna Array. *Nat. Commun.* **2011**, *2*, 267al.
51. Schnell, M.; Garcia-Etxarri, A.; Huber, A. J.; Crozier, K. B.; Borisov, A.; Aizpurua, J.; Hillenbrand, R. Amplitude- and Phase-Resolved Near-Field Mapping of Infrared Antenna Modes by Transmission-Mode Scattering-Type Near-Field Microscopy. *J. Phys. Chem. C* **2010**, *114*, 7341–7345.
52. Alonso-González, P.; Albella, P.; Schnell, M.; Chen, J.; Huth, F.; García-Etxarri, A.; Casanova, F.; Golmar, F.; Arzubiaga, L.; Hueso, L.; *et al.* Resolving the Electromagnetic Mechanism of Surface-Enhanced Light Scattering at Single Hot Spots. *Nat. Commun.* **2012**, *3*, 684.
53. McLeod, A.; Weber-Bargioni, A.; Zhang, Z.; Dhuey, S.; Harteneck, B.; Neaton, J. B.; Cabrini, S.; Schuck, P. J. Nonperturbative Visualization of Nanoscale Plasmonic Field Distributions *via* Photon Localization Microscopy. *Phys. Rev. Lett.* **2011**, *106*, 037402.
54. Carminati, R.; Nieto-Vesperinas, M.; Greffet, J.-J. Reciprocity of Evanescent Electromagnetic Waves. *J. Opt. Soc. Am. A* **1998**, *15*, 706–712.
55. Jackson, J. D. *Classical Electrodynamics*, 3rd ed.; Wiley: New York, 1998.
56. Collin, R. E. *Field Theory of Guided Waves*; Oxford University Press: New York, 1990.
57. Landau, L. D.; Lifshitz, E. M. *Electrodynamics of Continuous Media*; Pergamon Press: New York, 1963.
58. Schwinger, J.; Deraad, L., Jr.; Milton, K.; Tsai, W.; Norton, J. *Classical Electrodynamics*; Westview Press, 1998.
59. Nye, J. *Physical Properties of Crystals: Their Representation by Tensors and Matrices*; Oxford University Press: New York, 1957.
60. Marathay, A. S. Fourier Transform of the Green's Function for the Helmholtz Equation. *J. Opt. Soc. Am.* **1975**, *65*, 964–965.
61. Devaney, A. J.; Wolf, E. Multipole Expansions and Plane Wave Representations of the Electromagnetic Field. *J. Math. Phys.* **1974**, *15*, 234–244.
62. Kvien, K. Angular Spectrum Representation of Fields Diffracted by Spherical Objects: Physical Properties and Implementations of Image Field Models. *J. Opt. Soc. Am. A* **1998**, *15*, 636–651.
63. Johnson, P. B.; Christy, R. W. Optical-Constants of Noble-Metals. *Phys. Rev. B* **1972**, *6*, 4370–4379.